ISSN (Print) 1226-1750
ISSN (Online) 2233-6656
Journal of Magnetics 28(4), 374-384 (2023) https://doi.org/10.4283/JMAG.2023.28.4.374

Research on the Characteristics of AC Copper Loss and Suppression Method in Slotless Permanent Magnet Motor

Chenglong Chu and Yunkai Huang*

School of Electrical Engineering, Southeast University, Nanjing 210096, China

(Received 27 December 2022, Received in final form 30 October 2023, Accepted 6 November 2023)

Due to the absence of magnetic teeth on the stator to restrict the magnetic field, the windings of the slotless motor are directly exposed to the air gap magnetic field. Consequently, this exposure results in a more irregular distribution of current in the windings and a notable increase in AC loss. Therefore, it is the key point in the design of slotless permanent magnet motor (SPMM) to study the characteristics of AC copper loss in detail and the effective suppression method. According to the structural characteristics of SPMM, this paper proposes to reduce the gap between wires (WDG) to reduce the AC copper loss. And the corresponding winding production method - winding extrusion potting (WEP) for toroidal windings is also introduced. In addition, the measurement method of WDG is demonstrated through experiments, and the accurate value of WDG before and after using this suppression method are obtained. The research results indicate a 46 % reduction in AC copper loss attributed to circulating current. Ultimately, the experimental outcomes of the prototype align well with the theoretical analysis and computational findings.

Keywords : AC copper loss, circulating current, magnet-induced loss, slotless permanent magnet motor (SPMM), wire distance gap (WDG), winding extrusion potting (WEP)

1. Introduction

Due to its superior efficiency, high power density, and effective control capabilities, the permanent magnet synchronous motor (PMSM) is experiencing growing utilization in electric and hybrid vehicles, solar-powered aircraft, aircraft, compressor pumps, and various other applications [1, 2]. The increasing electrification of the transportation sector necessitates higher motor power density [3].

Wide bandgap devices such as Silicon Carbide (SiC) and Gallium Nitride (GaN) offer the potential to enhance efficiency, reduce drive size, and minimize passive device dimensions [4]. It also allows the motor to be designed with a larger number of pole pairs and operating frequency to achieve higher power density. However, the slotting effect in PMSM can result in cogging torque and torque ripple, limiting their application in scenarios requiring low vibration, low noise, and high reliability [5]. Therefore, in the design process, it is important to consider the traditional stator teeth-slots structure to prevent saturation and minimize iron loss. Fortunately, these drawbacks are circumvented by the use of Surface Permanent Magnet Motors (SPMM).

Whereas, compared with slotted motors, windings used in slotless motors account for a higher proportion. Since the stator core does not get the restriction of the teeth structure on the magnetic field, windings are directly exposed to the armature magnetic field and the PM field [3]. Under the action of AC excitation, the skin effect and proximity effect cause uneven distribution of current density within the conductor, leading to a decrease in the equivalent current-carrying area and resulting in additional copper loss (Strand-level loss) [6, 7].

Furthermore, the stator winding is typically constructed by multiple conductors with smaller diameters, resulting in a larger total equivalent area for each coil. This can lead to variations in the positions of the conductors and the magnetic flux of each turn of the parallel strands, ultimately causing asymmetry in inductance [8].

The uneven distribution of the field in the region encompassed by the various parallel strands leads to variations in the amplitude and phase of the current in each strand within a single bundle, resulting in significant

*Corresponding author: Tel: +8602583791696
Fax: +8602583794169, e-mail: huangyk@seu.edu.cn

AC copper loss (Bundle-level loss). The AC copper loss in windings is closely associated with the amplitude and frequency of the current. The skin effect, proximity effect, and the unequal current in the parallel strands all contribute to increasing AC copper loss to varying degrees. Current literatures predominantly focus on the computation and distribution characteristics of AC copper loss in motors [3, 9]. In slotted motors, partially filling the slot is employed to mitigate AC copper loss stemming from magnetic flux leakage. Furthermore, in addressing the issue of substantial AC copper loss in hairpin winding flat wire motors [10], proposes the use of formed transposition windings in PMSM.

The most commonly employed method for suppression involves selecting the appropriate wire diameter and number of parallel strands [11]. However, these methods have certain limitations and drawbacks. The conductor diameter cannot be minimized without encountering difficulties in winding. The benefits of parallel strands are constrained by uneven current distribution among the strands [12]. Partially filling the slot decreases the slot filling rate and increases the motor volume, thereby impacting the motor's power density [13]. Furthermore, while the use of litz wire is known to reduce AC copper loss, its high cost presents challenges for implementation in cost-constrained applications. In [14], it was suggested that AC copper loss can be mitigated by controlling the position of the conductors within the slot, but the suppression method described in this paper is deemed to be lacking in operability and challenging to implement.

This paper presents a method for mitigating AC copper loss in slotless motors. The primary focus of the paper includes identifying the sources of loss in the inner and outer layer windings, with a particular emphasis on bundle-level loss as the primary component of AC loss. The proposed suppression method is introduced, along with the corresponding winding production technique of winding extrusion potting. This method is more practical compared to other approaches found in existing literature. Furthermore, it is demonstrated that the proposed method can enhance the equivalent thermal conductivity of the windings and improve their heat dissipation capacity. The paper also determines the equivalent winding distribution factor (WDG) of the windings produced by the proposed method through calculations and comparisons of magnet-induced loss values from several sets of open circuit experiments. The experimental results indicate that this method can reduce bundle-level loss by 46 %, effectively suppressing AC copper loss.

2. Investigated Machine and The Impact of Different Magnetic Fields

2.1. Investigated Machine

The slotless motor commonly utilizes windings attached to the inner stator core and toroidal windings wound along the axial direction. The different winding structures are depicted in Fig. 1. In the conventional winding, the two effective parts are positioned between the stator core and the rotor, whereas in the toroidal winding, the two effective parts are located on the inner and outer sides of the stator core. Consequently, the AC copper loss of conventional windings can be compared to the AC copper loss characteristics of the inner winding. To comprehensively investigate the AC copper loss in the winding of the SPMM, this study focuses on the slotless motor with toroidal winding as an example for research.

The prototype described in this paper features a slotless stator with toroidal windings. The 3D model and cross-sections of the prototype are depicted in Fig. 2, and relevant design parameters are listed in Table 1. The SPMM has 12-teeth/10-poles, the turns number of coils is 25, and each turn is wound by 15 conductors with diameter of 0.6 mm. To protect the Halbach permanent

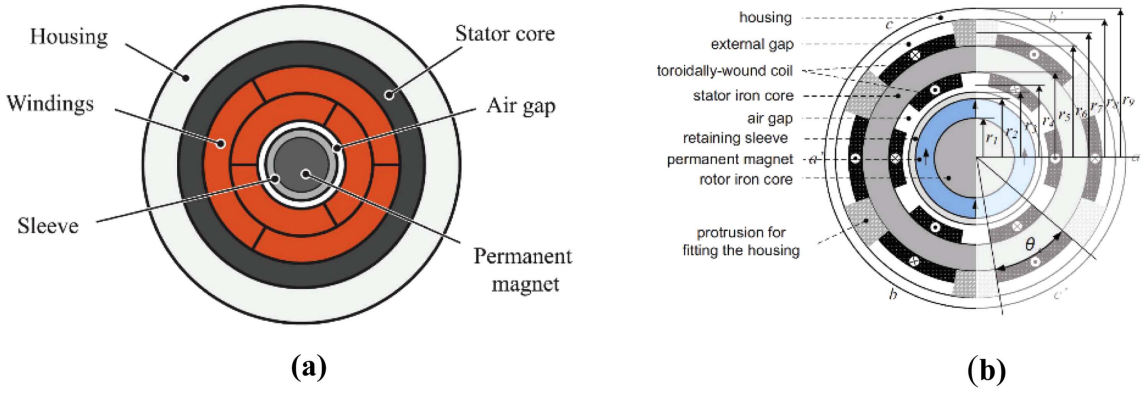

Fig. 1. (Color online) Different winding structures in the literature. (a) Conventional windings. (b) Toroidal windings.

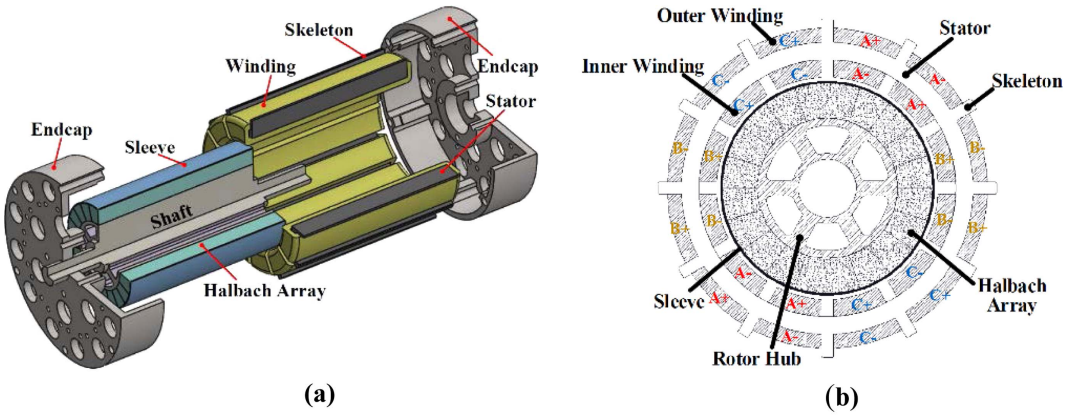

Fig. 2. (Color online) The model of prototype. (a) 3D. (b) cross-section.

Table 1. Design parameters of the SPMM.

Number of poles	10	Number of slots	12
Power (kW)	3.0	Rated/Max speed (r/min)	1000/6000
PM thickness (mm)	18	Rated current (A)	30
Stator stack length (mm)	180	Physical air gap (mm)	2

magnet array attached to the rotor surface, a carbon fiber sleeve is employed in the rotor. The toroidal windings are arranged in multiple ring structures around the inner and outer sides of the stator core, resulting in a significant reduction in the length of end windings and the axial installation size of the SPMM [17].

The calculation of AC copper loss requires precise modeling of each conductor. The placement and position of the conductors in each turn should be as close as possible to the actual windings. In toroidal winding, the winding area of a coil is determined based on the number of slots. The winding is generally started from one side of the area and wound around the stator core to the other side. So, there are multiple layers of windings. In the analysis model, bundle positions and numbers of the inner and outer windings are shown in Fig. 3. Based on the distance between the position of each turn and the center of the motor, the outer and inner windings can be categorized into three layers and four layers, respectively.

2.2. The Impact of Different Magnetic Fields

When the motor is running at rated speed, the current density distribution of the windings is shown in Fig. 3. In order to accurately determine the AC copper loss, it is

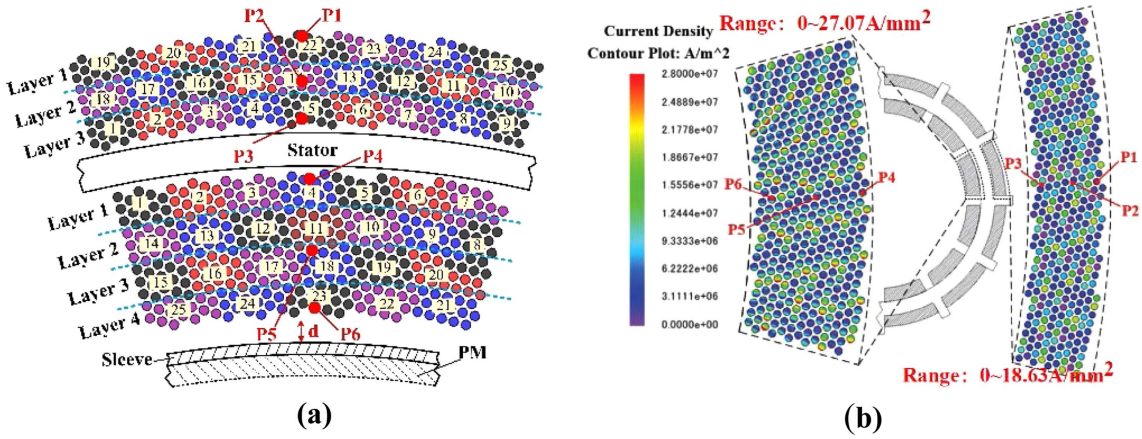

Fig. 3. (Color online) Bundle positions and numbers of the inner and outer windings. (a) Positions. (b) Current distribution.

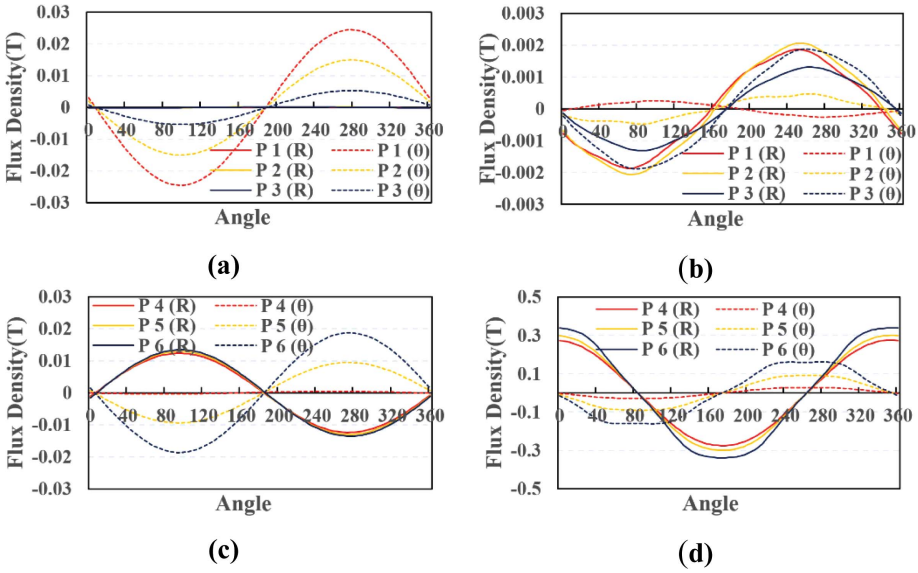

Fig. 4. (Color online) Radial and tangential flux density waveforms of different sampling points at rated state. (a) Outer-ArmatureOnly. (b) Outer-PMOnly. (c) Inner-ArmatureOnly. (d) Inner-PMOnly.

essential to create a model for each conductor and incorporate an external circuit for connection with FEM. To expedite the calculation process, modeling only half of the motor based on symmetry can be employed. Furthermore, the modeling will focus on all conductors within a single coil, and the overall AC copper loss can be derived from the cumulative loss values obtained in this modeling component. It is important to note that the inner winding exhibits a substantially higher maximum induced current density compared to the outer winding, with values of 27.07 A/mm^2 and 18.63 A/mm^2, respectively, in the instantaneous state. Furthermore, the current density distribution on each conductor in the outer winding is nearly uniform. In contrast, the current density within the conductor of the inner winding varies significantly with the rotor position. This indicates that the sources of AC loss in the inner and outer windings are distinct.

The magnetic field surrounding the windings is a result of the interaction between the armature magnetic field and the PM field. The distribution of flux density in the windings plays a crucial role in determining the extent and distribution of AC copper loss. Consequently, the frozen permeability method is employed to individually evaluate the impact of the two magnetic fields on AC copper loss. In Fig. 3(b), six sampling points selected in different radius of outer windings and inner windings area to observe the radial R and tangential θ magnetic density curves of sampling points in an electrical cycle, as shown in Fig. 4. Where "Outer-ArmatureOnly" indicates that Outer windings are Only affected by Armature magnetic field, and other symbols have similar meanings.

Comparing Fig. 4(a) with (c), it is observed that the flux density at various sampling points of the inner and outer windings is relatively similar when only the armature magnetic field is applied. If the PM field is applied alone, as shown in Fig. 4(b) and (d), maximum flux density at sampling points of inner windings is much greater than that of the outer windings. Consequently, the primary cause of the AC copper loss in the outer windings is attributed to the armature magnetic field, while the inner windings are predominantly affected by the PM field.

Moreover, by comparing Fig. 4(c) and (d), it can be seen that the flux density amplitude is significantly higher when only a PM field is applied to the inner winding. Meanwhile, for Fig. 4(d), the flux density amplitude of three points is different. The proximity of the sampling point to the rotor correlates with an increase in the magnitude of magnetic flux density. The analysis above indicates that the inner winding is directly influenced by the magnetic field of the air gap, leading to varying magnetic flux density distributions across the conductors within the winding due to the permanent magnetic field. Consequently, this disparity results in the generation of circulating current and noticeable AC copper loss. For the SPMM with conventional winding, the relative position of the winding is the same as that of the inner winding of toroidal windings, so the comparative analysis results of Fig. 4(c) and (d) are also applicable.

3. The Suppression Method of AC Copper Loss for Slotless Motor

3.1. Model for Assessing the Effect of Circulating Current

In FEA, separate current sources are applied to parallel strands to eliminate the influence of uneven current distribution caused by magnetic field, and the quantitative analysis of the influence of circulating current on AC copper loss is realized [14]. Fig. 5 shows the circuit setting in different conditions. In Fig. 5(a), multiple parallel strands are supplied by the single current source (SCS), which is also the circuit state of the motor in actual operation. Fig. 5(b) shows that each conductor is excited by an individual current source (ICS). In this way, the circulating current in the winding can be eliminated and the effect of different magnetic field can be ignored. Certainly, ICS has the same frequency as SCS and its amplitude is 1/15 times that of SCS. In the former case, the AC copper loss calculated includes DC component, strand-level loss and bundle-level loss, and the bundle-level loss is eliminated in the latter case.

The current waveform in each conductor is shown in Fig. 6(a). Due to the evident discrepancies in current amplitude and phase among parallel bundles, there will be additional losses at the bundle level in the windings. To prevent the disorderly arrangement of 15 current waveforms and facilitate a more distinct assessment, FFT analysis is conducted. The amplitude of the rated frequency, and total harmonic distortion (THD) are shown in Fig. 6(b). Because the larger these two numbers are, the greater the AC copper loss in a single conductor will be under this current waveform. The red label of the current amplitude of each parallel strand is the corresponding THD results. The THD of the current waveform can also be used as an index to judge AC copper loss, because according to (1), it can be known that the current frequency is positively correlated with AC copper loss [18].

$$P_{strand} = \frac{\pi \omega_e^2 l_{eff} d^4 B^2}{128 \rho_{cu}} \tag{1}$$

where ω_e is the excitation, ρ_{cu} represents the electrical resistivity of copper, l_{eff} is the effective length of the conductor, d is the strand diameter, and B is the flux density amplitude at the strand location in the slot.

Obviously, there is a notable disparity in the current waveform of each parallel conductor. The results of the

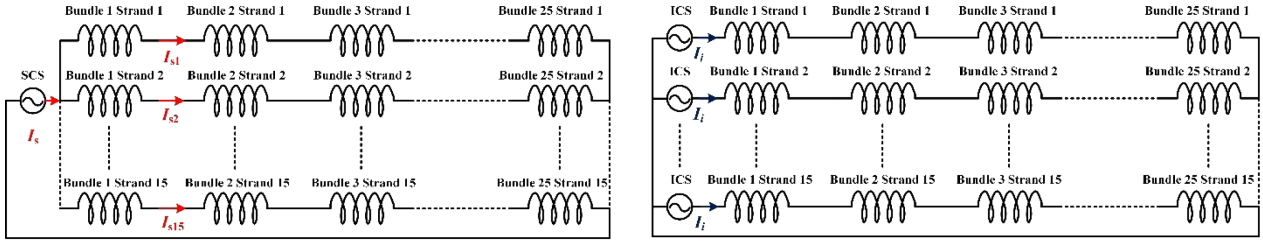

(a) (b)

Fig. 5. (Color online) Different circuit settings for separating bundle-level loss. (a) Single current source. (b) Individual current source.

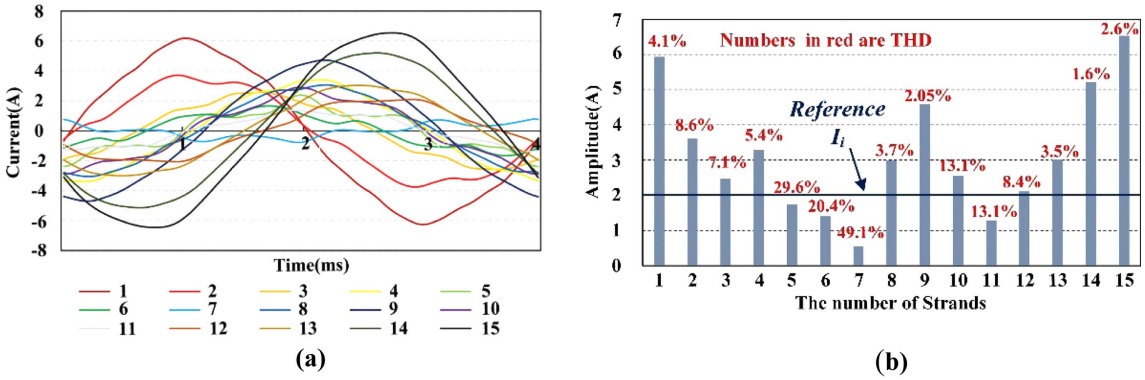

(a) (b)

Fig. 6. (Color online) Waveforms of individual strand currents and results of FFT (by using the SCS). (a) Waveforms. (b) Amplitude of the fundamental component and THD in %.

Fast Fourier Transform (FFT) analysis indicate that the fundamental amplitude of each waveform varies between 0.54 A and 6.5 A, with the maximum value being 3.25 times the reference value of 2 A. As copper loss is directly proportional to the square of the current, the higher amplitudes result in a substantial AC copper loss.

Different types of copper losses can be distinguished by comparing the computed results from two scenarios. In this case, the DC copper loss, strand-level loss, and bundle-level loss are determined to be 191.7 W, 36.5 W, and 368.2 W, respectively. The relatively low strand-level loss is attributed to the appropriate selection of conductor diameter, while the bundle-level loss constitutes over 60 % of the total copper loss. This indicates that, for a specific conductor diameter, the AC copper loss in windings is influenced by the circulating current between parallel strands.

3.2. The Proposed Suppression Method of AC Copper Loss

In slotted motors, the winding is generally put into the stator slot from the slot opening. It is difficult to control the WDG along the axial direction of the motor between the conductors in the slot. However, in SPMM, the entire coil can be readily accessed. Therefore, based on the structural features of the slotless motor, this study suggests a technique for mitigating AC copper loss by minimizing the winding. In the assessment and simulation of AC copper loss, the focus is typically on the bare conductor while the insulation is not taken into account. Consequently, to align with the electromagnetic model, the winding represents the combined thickness of the insulating layers of two conductors and the physical air gap between them. The structural illustration of the winding is depicted in Fig. 7.

A comparative examination is conducted on three states of WDG with thicknesses of 0.2 mm, 0.1 mm, and 0.05 mm. It is evident that the WDG with a thickness of 0.05 mm is considered optimal and is solely utilized to assess the impact of this suppression technique. The primary amplitude and total harmonic distortion (THD) of the individual current under these three conditions are depicted in Fig. 8.

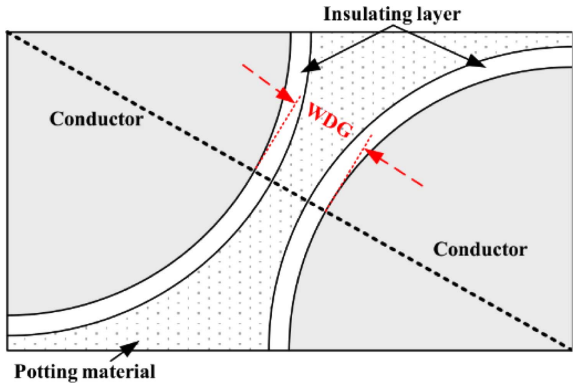

Fig. 7. (Color online) The definition of WDG.

Most obviously, when WDG decreased from 0.2 mm to 0.1 mm and 0.05 mm, the current amplitude in each conductor fluctuated from 0.54-6.5 A to 1.337-5.485 A (0.1 mm) and 1.311-4.341 A (0.05 mm), respectively. Furthermore, as WDG decreased, there was a significant decrease in the THD of the current waveform in parallel strands. Specifically, when WDG was reduced to 0.05 mm, the THD of the current waveform in all conductors was found to be less than 10 %.

The AC copper loss of each bundle in the inner and outer winding under different WDGs is calculated as shown in Fig. 9. It is evident that the AC copper loss for each bundle in both the inner and outer windings experiences a notable increase with the rise in WDG. Conversely, as the WDG decreases from 0.2 mm to 0.05 mm, the DC copper loss remains constant, the strand-level loss exhibits a slight increase, and the bundle-level loss decreases by approximately 55 % and 69 %, respectively.

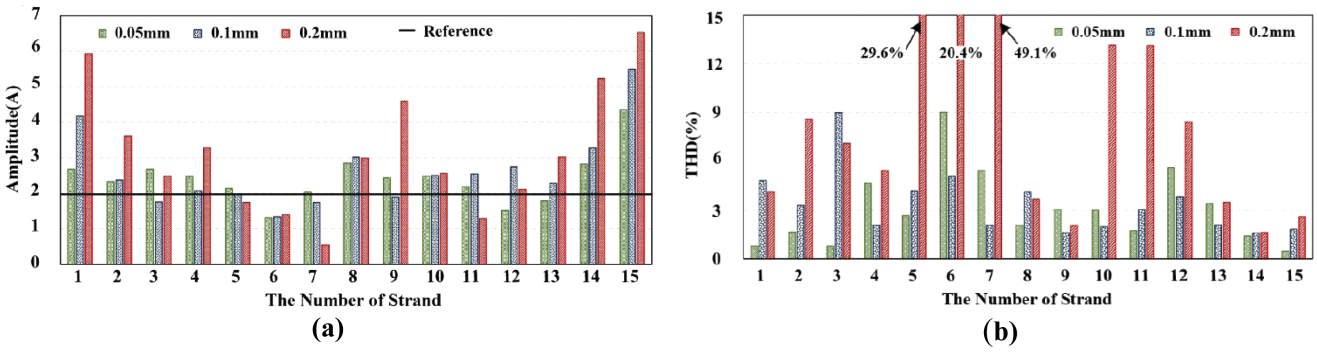

Fig. 8. (Color online) The amplitude and THD of single conductor current under different WDGs. (a) Amplitude. (b) THD.

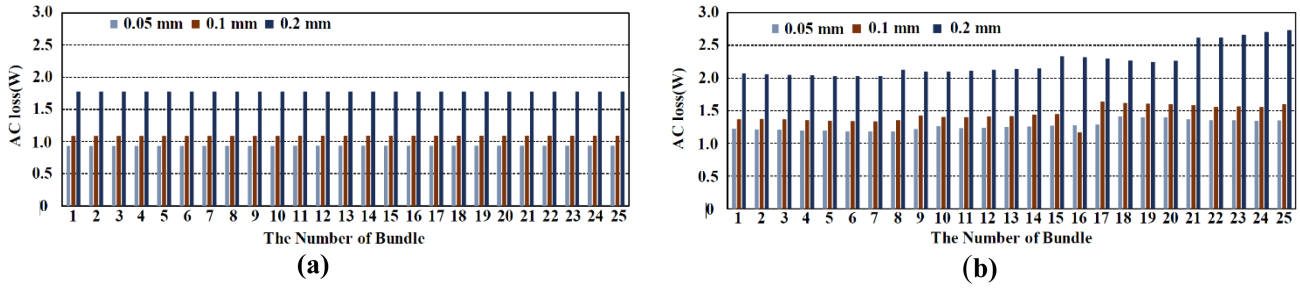

Fig. 9. (Color online) Comparation of the AC copper loss per turn under different WDGs. (a) Outer winding (b) Inner winding.

In slotted motors, controlling the WDG is challenging unless the stator is segmented. However, in slotless motors, this concept is highly achievable irrespective of the winding configuration. Prefabricated winding can be employed for conventional windings to effectively minimize the WDG. The subsequent section will present the manufacturing process of windings using this approach, focusing on toroidal winding.

4. The Manufacture Process and Obtaining the Equivalent WDG

4.1. The Manufacture Process

The winding extrusion encapsulation (WEP) winding production method utilizes a winding extrusion encapsulation process, which involves the application of external force to the winding during encapsulation. This results in a reduction in the distance between the conductors after the epoxy resin cures, leading to a significant decrease in circulating current and AC copper loss. Additionally, the reduced distance between the conductors contributes to the effective reduction of circulating current and AC copper loss after the epoxy resin cures.

The manufacturing process is shown in Fig. 10. The first image depicts a single coil, where the wire appears to be loosely wound and easily bent during the winding process, resulting in an increased distance between the conductors. In the second image, the extrusion and potting process is illustrated. The potting material, with good fluidity, effectively fills the gaps between the conductors through multiple extrusion and release. The presence of bubbles in this image indicates the presence of air within the winding at that time. As depicted in the third image, the disappearance of bubbles in the potting material after extrusion signifies the application of continuous extrusion to the entire winding until the potting material is fully cured. The fourth and fifth images reveal that, apart from the large gaps at the upper edge of the winding resulting from the cutting process, the distance between the conductors at other positions is relatively small.

4.2. The method for obtaining the equivalent WDG

While the manufacturing method described above can decrease the WDG between conductors, its ability to yield a precise WDG for the electromagnetic calculation model remains uncertain. This uncertainty arises from the inherent randomness in the winding process and the inherent disparities in the manufacturing process. Consequently, this section introduces a method for determining the precise equivalent WDG.

The approach of this technique involves determining the equivalent winding distribution factor (WDG) by comparing the magnet-induced loss of the measured winding with simulation outcomes. The magnet-induced loss refers to the eddy current loss in the stator windings

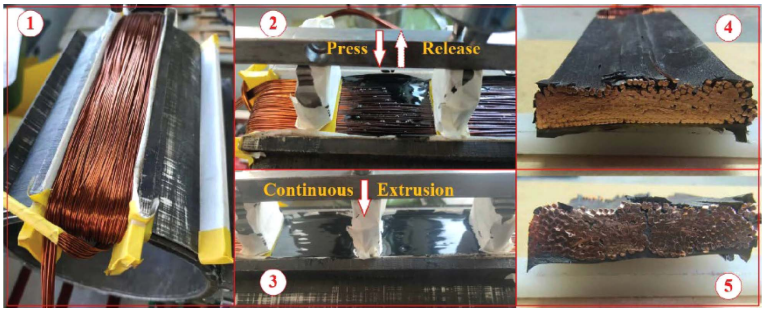

Fig. 10. (Color online) The production process of WEP.

resulting from the magnetic field when the rotor rotates passively in the open circuit state. This type of loss can be computed by considering the no-load loss, mechanical loss, and iron loss. The interrelation among these various losses is delineated as follows:

$$P_{no-load} = P_{mechanical} + P_{magnet-induced} + P_{iron} \quad \text{(a)}$$

where no-load losses include mechanical losses, magnet-induced loss and iron loss. It should be noted that the magnet-induced loss is the loss induced in conductors by the rotation of the PM field. Among them, no-load loss and mechanical loss can be accurately evaluated by test experiments.

In the study by [19], the no-load loss test examines the correlation between the deceleration rate of rotating components and the overall no-load loss that acts to slow them down. The no-load loss encompasses iron loss, magnet-induced loss in windings, and mechanical losses incurred during rotor rotation, such as air friction loss and bearing friction. Previous research has provided comprehensive formulas for air friction loss [20].

The determination of bearing loss is a complex process due to its dependence on various factors, including the type of bearing lubrication, load, speed, operating temperature, and rotor imbalance. Some models to calculate it, but they are not accurate enough. Empirical formulas derived from experimental tests or tools like the SKF online calculator can estimate rolling friction from applied load and viscous friction of the lubricating medium. However, the accuracy of these calculations is compromised by variations in working conditions and motor installation states. Consequently, while empirical formulas can provide a rough estimate of mechanical motor loss, including wind resistance and bearing friction loss, their accuracy is difficult to ensure.

5. Experimental Validation

5.1. Platform

The prototype's effective axial length is 180 mm, and due to the substantial weight of the rotor, achieving higher speeds poses a challenge. To compare the suppression effect of the method proposed in this study on the equivalent Winding Distribution Generator (WDG), magnet-induced loss, and AC copper loss, a new stator winding is fabricated using the extrusion potting method, and a corresponding rotor is paired with it, as depicted in Fig. 11(a). Notably, the effective length of the stator core matches the effective length of the permanent magnet at 50 mm, while the rotor length measures 80 mm. Additionally, an Inconel 718 alloy sleeve with a 1.5 mm thickness is employed to safeguard the PM.

In order to obtain the equivalent WDG of the winding before and after extrusion potting, multiple experiments are carried out. The test platform is shown in Fig. 11(b). The drive motor is coaxially connected with the torque sensor and the rotor shown in Fig. 11(a). The rotor runs at different speeds under the drag of the driving motor. The value of the torque sensor corresponds to the output power of the drive motor. Taking into account the existence of bearing friction loss under different installation conditions, and results are averaged through multiple test experiments to obtain more accurate mechanical loss. It should be noted that Fig. 11(b) contains the test contents of three different CASEs:

No winding: Only the rotor is installed on the right side of the torque sensor. Therefore, the value of torque sensor only reflects mechanical losses, including bearing friction

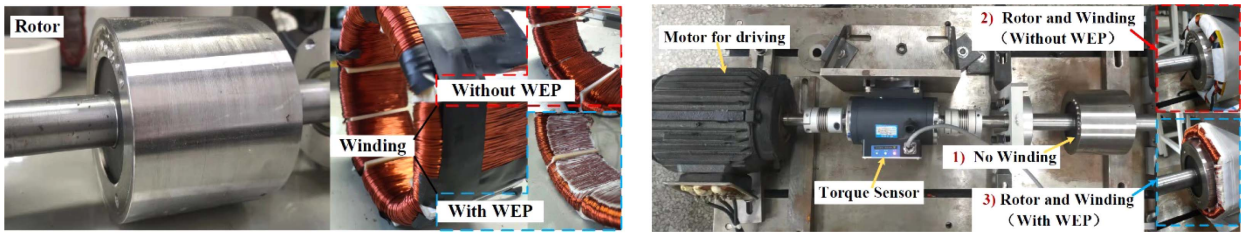

(a) (b)

Fig. 11. (Color online) Test platform for measuring no-load loss and mechanical loss. (a) stator and rotor. (b) Test platform.

Table 2. The Average Torque of different cases.

	3000 r/min	6000 r/min	9000 r/min	12000 r/min
Case 2)-N.m	0.215	0.255	0.282	0.318
Case 3)-N.m	0.197	0.237	0.265	0.298

loss and air friction loss. To accurately determine the iron loss, the stator core (without winding) is subsequently incorporated into the testing process, and the disparity between the two sets of test results is analyzed.

Rotor and Winding (Without WEP): Subsequently, following the installation of the rotor, the stator component is also installed, although the winding has not yet been implemented using the WEP method. The torque sensor's measurement reflects the combined effects of mechanical loss and magnet-induced loss within the winding.

Rotor and Winding (With WEP): The experimental setup closely resembles CASE 2, with the exception that the windings are fabricated using WEP.

Furthermore, the FEA value of iron loss may be significantly underestimated as a result of diverse manufacturing factors, contingent upon the technique employed to cut the laminate from the blank. Consequently, it is imperative to take into account a build factor. The accuracy of the chosen construction factor may be compromised, thereby exerting a substantial impact on the precision of the ultimate conclusion. In scenario 2, two experiments are carried out to determine the actual iron loss of the prototype before and after. The disparity in iron loss between the two tests is then assessed. The sum of mechanical loss and $P_{magnet-induced}$ can be calculated by the difference between the experimental results of Case 2), 3) and the iron loss as shown in Fig. 11, and then the mechanical loss obtained by Case 1) can be subtracted to obtain $P_{magnet-induced}$. So more accurate loss values are obtained through experiments in this paper.

6. Results and Analyses

The driving motor accelerates the entire system from a stationary state to 12000 r/min. Recording points are selected at 3000, 6000, 9000, and 12000 r/min, and the system runs at each speed point for a specific duration to obtain a relatively stable torque value. Fig. 12(a) and (b) depict the torque sensor readings at different speeds in CASE 2) and 3), with detailed values presented in Table 2. Subsequently, the output power of the driving motor can be computed. The discrepancy between the resultant power and the mechanical loss represents the magnet-induced loss in the winding.

It can be seen that the torque measured at each rotating speed point in CASE 3) is smaller than that in CASE 2). Since the mechanical losses of CASE 2) and CASE 3) are consistent, the magnetic-induced loss of CASE 3) is significantly smaller than that of CASE 2). The specific values of different losses are shown in Fig. 13(a), and the losses all increase with the increase of rotation speed.

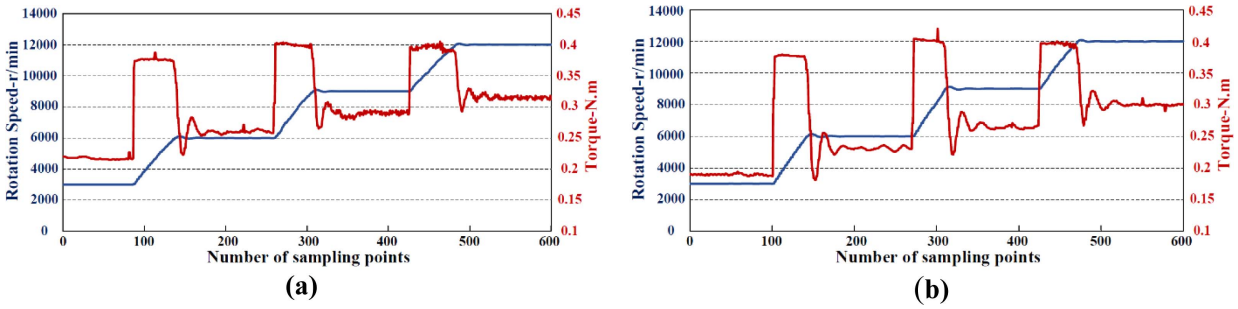

Fig. 12. (Color online) Torque and speed data sampled under different conditions. (a) Case 2). (b) Case 3)

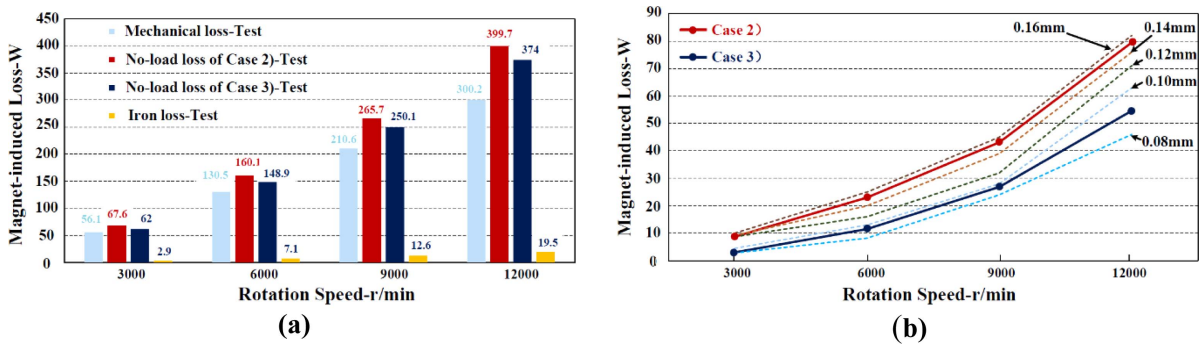

Fig. 13. (Color online) Losses at different speeds. (a) Comparison. (b) Magnet-induced loss.

Table 3. The Magnet-induced Loss of different cases.

	3000 r/min	6000 r/min	9000 r/min	12000 r/min
Case 2)-W	8.6	22.5	42.5	80.0
Case 3)-W	3.0	11.3	26.9	54.3

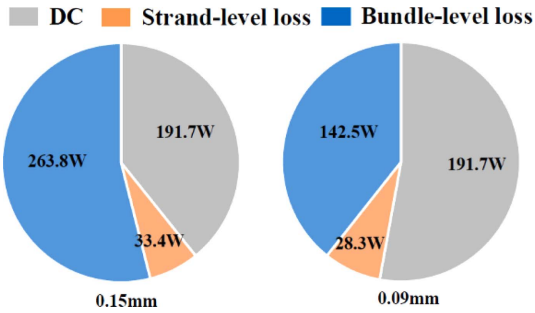

Fig. 14. (Color online) The loss comparison of various sources under different WDGs.

Then, through simple calculation, more accurate WDG can be obtained under different conditions.

According to (2), the magnet-induced loss of different cases is shown in Table 3. It can be seen that magnetic-induced loss increases with speed and the increments are more obvious with the increase of speed. In addition, the magnetic-induced loss of CASE 3) is significantly lower than that of CASE 2), indicating that magnetic-induced loss is effectively reduced by the application of the WEP method.

The magnetic-induced loss values, both measured and calculated, are depicted in Fig. 13(b). Each dashed line represents the calculated data for different winding (WDG) settings. These lines illustrate the variation of magnet-induced loss with speed under different WDG configurations.

It is evident that the magnet-induced loss for CASE 2) at different speeds, as determined by the test results, falls within the upper and lower limits of the results when WDG is set between 0.14 mm and 0.16 mm. Consequently, the equivalent WDG for CASE 2) is deemed to be 0.15 mm. Similarly, the equivalent WDG for CASE 3) is considered to be 0.09 mm.

Subsequently, the corresponding WDG in the FEM is established as 0.15 mm and 0.09 mm, and the loss at the bundle level is segregated based on the circuit configurations depicted in Fig. 5. The computed loss outcomes are presented in Fig. 14. As the WDG diminishes, the DC copper loss remains constant, the loss at the strand level experiences a slight reduction, and the loss at the bundle level decreases by 46 %. This indicates that the reduction in WDG effectively diminishes the circulating current in the conductors, leading to a substantial decrease in AC copper loss.

7. Conclusion

This paper provides a detailed examination of the characteristics of AC copper loss in SPMM and proposes an effective method for mitigating this loss. Regardless of the winding structure employed in SPMM, the windings in the air gap are directly exposed to the magnetic field, leading to uneven magnetic flux density distribution and resulting in noticeable circulation and AC copper loss. Quantitative analysis reveals that the AC copper loss of the inner winding in toroidal winding is significantly higher than that of the outer winding. Furthermore, the bundle-level loss caused by circulating current is found to exceed 50 % of the total AC copper loss and can be mitigated through different circuit settings.

This paper proposes the method of reducing the circulating current by reducing the WDG to suppress the AC copper loss. Moreover, winding extrusion potting method for toroidal winding is introduced and analyzed. Furthermore, a method for accurately determining the WDG is proposed. The equivalent WDG is determined by comparing the calculated magnet-induced loss with experimental findings. The outcomes demonstrate a 46 % reduction in bundle-level loss following the implementation of this loss suppression approach.

References

[1] B. Guo, Y. Huang, F. Peng, and J. Dong, IEEE Trans. Ind. Electron. (2019) pp. 5015-5024.
[2] Y. Tang, F. Chai, and L. Chen, IEEE Trans. Transport. Electrific. (2022) pp. 1085-1093.
[3] M. S. Islam, R. Mikail et al., IEEE Trans. Ind. Appl. (2019) pp. 5789-5799.
[4] J. Millinger, O. Wallmark et al., IEEE Trans. Ind. Electron. (2020) pp. 6280-6289.
[5] Z. Song, C. Liu et al., IEEE Trans. Transp. Electrif. (2020) pp. 1577-1591.
[6] F. Chai, Z. Li, Y. Pei, Y. Shao, and M. Hu, IEEE Trans. Transport. Electrific. (2021) pp. 2812-2821.
[7] P. B. Reddy and T. M. Jahns, 2010 International Power Electronics Conference -ECCE ASIA, 2010.
[8] X. Fan, D. Li et al., 20th International Conference on

Electrical Machines and Systems (ICEMS), 2017.
[9] A. Al-Timimy, P. Giangrande et al., 2018 XIII International Conference on Electrical Machines (ICEM) (2018) pp. 263-269.
[10] Y. Liang F. Zhao et al., IEEE Access, (2021) pp. 101105-101114.
[11] D. A. Gonzalez and D. M. Saban, IEEE Trans. Ind. Electron. (2014) pp. 3038-3045.
[12] P. B. Reddy and T. M. Jahns, The 2010 International Power Electronics Conference -ECCE ASIA, (2010) pp. 2181-2188.
[13] M. van der Geest, H. Polinder, J. A. Ferreira, and D. Zeilstra, 2013 International Electric Machines Drives Conference, (2013) pp. 340-346.
[14] A. Bardalai, D. Gerada et al., IEEE Trans. Ind. Appl. (2020) pp. 183-193.
[15] A. Tüysüz, F. Meyer, M. Steichen, C. Zwyssig, and J. W. Kolar, IEEE Trans. Ind. Appl. (2017) pp. 2077-2087.
[16] A. Borisavljevic, S. Jumayev, and E. Lomonova, International Conference on Electrical Machines, 2014.
[17] J. Dong, Y. Huang et al., IEEE Trans. Magn. (2014) pp. 1-4.
[18] Reddy, Patel. B., Jahns, Thomas. M., and Bohn, Theodore. P, IEEE Energy Conversion Congress and Exposition, (2009) pp. 1919-1926.
[19] D. M. Saban, C. Bailey et al., 56th Annual Petroleum and Chemical Industry Conference, (2009) pp. 1-9.
[20] J. Saari, Ph.D. Thesis, Helsinki University of Technology, 1998.